Seasonal variations of the nighttime O(^{1}S) and OH airglow emission rates at mid-to-high latitudes in the context of the large-scale circulation

Guiping Liu,[1,2] Gordon G. Shepherd,[1] and Raymond G. Roble[3]

[1]Centre for Research in Earth and Space Science, York University, Toronto, Ontario, Canada M3J 1P3.

[2]Now at Air Quality Research Division, Environment Canada, 4905 Dufferin Street, Downsview, Ontario, Canada M3H 5T4

[3]High Altitude Observatory, National Center for Atmospheric Research, Boulder, Colorado, CO 80307, USA.

Abstract

The seasonal climatology of the O(^{1}S) and OH nighttime airglow in the mesosphere and lower thermosphere (MLT) for the mid-to-high latitude region is explored in the context of the large-scale general circulation. Multiple years of the Wind Imaging Interferometer (WINDII) satellite data during November 1991-August 1997 are monthly averaged to depict the global patterns of the seasonal variations of the airglow volume emission rates for various altitudes and local times. These observations are compared with the simulations of the Thermosphere-Ionosphere-Mesosphere Electrodynamics General Circulation Model (TIME-GCM). Both the WINDII and the TIME-GCM results display the semi-annual and annual variations of the O(^{1}S) and OH airglow emission rates for specific altitudes and local times. The TIME-GCM reproduces most of the emission variation signatures observed by WINDII, but provides additional information on vertical winds and downward mixing of atomic oxygen. The study indicates that the vertical advection associated with the tides and the large-scale circulation plays a major role in the airglow seasonal variations. The influence of the large-scale circulation appears more clearly in the mesosphere than in the lower thermosphere, while the semi-annual variation occurs only in the lower thermosphere. A superimposed summer peak in the annual variation of the OH emission rate appears to result from an enhanced diffusion rate at that season.

1. Introduction

The nighttime O(^{1}S) and OH airglow emissions in the mesosphere and lower thermosphere (MLT) originate from the recombination of atomic oxygen (e.g. review by McDade and

Llewellyn, 1986; McDade et al., 1987; Meriwether, 1989). Atomic oxygen is produced through the photo-dissociation of molecular oxygen in the thermosphere, and its global distribution in the MLT region is mainly controlled by dynamical transport processes (e.g. Brasseur and Solomon, 1986; Garcia and Solomon, 1985). Variations of the $O(^1S)$ and OH airglow emission rates shed insights on wave activity and on large-scale transport of atomic oxygen in the region (e.g. Taylor et al., 1995; Makhlouf et al., 1997; Shepherd et al., 1995; McLandress et al., 1996; Yee et al., 1997; Shepherd et al., 2005).

From temperature measurements it is well known that the mean general circulation in the mesosphere includes an upward motion in summer and a down-welling during winter for high-latitudes (e.g. Andrews et al., 1987). The large-scale circulation is also expected to bring atomic oxygen-poor air from below and atomic oxygen-rich air from above, causing a decrease of the atomic oxygen airglow emission rate in summer and an enhancement of the emission rate during winter. Therefore, an annual variation of the $O(^1S)$ and OH nightglow emission rate for mid-to-high latitudes is expected. However, as shown by the results reported here, the situation is more complex than that.

The variation of the $O(^1S)$ airglow emission rate was first recognized by Rayleigh in 1928 (Rayleigh, 1928), and since then the airglow variability has been studied for a long time using both ground-based and space-borne observations. An extensive review of long-term observation data from various ground stations shows that the seasonal variations of the $O(^1S)$ nightglow are globally dependent, having different patterns at different latitudes (Deutsch and Hernandez, 2003). The emission exhibits a distinct semi-annual behavior for the equator and tropics with emission rate maximums at equinoxes and minimums during solstices (e.g. Fukuyama, 1977; Takahashi et al., 1995). In the mid-to-high latitude region away from the equator, both semi-annual and annual oscillations have been identified (e.g. Fukuyama, 1977; Hecht et al., 1997). Moreover, it has been found that the amplitude of the annual component increases with latitude while the semi-annual variation amplitude decreases with latitude (Deutsch and Hernandez, 2003). The seasonal variation is also evident in space-borne observations. OGO satellite data have shown a strong semi-annual pattern in the $O(^1S)$ emission rate, with the largest values in April and October (Donahue et al., 1973). Analysis of the ISIS-II satellite data has also indicated a semi-annual variation in the $O(^1S)$ emission for the mid-latitude region (Cogger et al., 1981).

Ground-station observations are limited to specific geophysical locations, but the observations are nearly continuous in time for a given day. Satellites can obtain a global picture of the emission variations, but their measurements on a single day for a given latitude normally cover a segment of local time of only a few minutes. Furthermore, ground-based instruments measure the airglow integrated emission rates from the whole emission layer. Limb-viewing satellite instruments such as WINDII (Wind Imaging Interferometer) on UARS (Upper Atmosphere Research Satellite) have the advantage of observing the vertical profiles of the airglow volume emission rates. The airglow variations for various altitude levels in different latitude regions over the whole globe are easily discerned from the satellite data. To interpret and understand the observations, numerical model simulations are required. Global general circulation models that incorporate photochemistry and dynamics for the production of the oxygen airglow emissions are essential to study this large-scale variability.

Some previous model studies have proposed that the semi-annual variation of atomic oxygen and oxygen airglow is due to seasonal changes in eddy diffusion caused by gravity wave dissipation (e.g. Garcia and Solomon, 1985). However, those authors assumed that higher eddy diffusivity produces reduced airglow emission (by downward mixing out of the airglow region) which is opposite to what is currently believed. Recently, vertical advection associated with the tides has been shown to be the primary mechanism for the diurnal variation of the $O(^1S)$ airglow at the equator (e.g. Angelats I Coll and Forbes, 1998; Ward, 1999). More recent analysis of the NCAR (National Center for Atmospheric Research) TIME-GCM (Thermosphere Ionosphere Mesosphere Electrodynamics General Circulation Model) simulations has suggested that for mid- and high latitudes the vertical advection of the mean circulation cell dominates the transport of atomic oxygen and diffusive and meridional transport have a secondary effect (Liu and Roble, 2004). The relative importance of vertical advection and turbulent mixing on the transport of atomic oxygen may be assessed from the variations of the oxygen airglow emission rates by employing numerical model simulations.

These studies are reinforced by a recent comparison of the SABER/TIMED satellite observations with a three-dimensional chemical dynamical model, showing that the diurnal tide has a large effect on the low-latitudinal OH emission variation (Marsh et al., 2006). The study also shows that the annual cycle of the emission at higher latitudes is mainly caused by the reversing mean circulation. The $O(^1S)$ emission occurs at a higher altitude than the OH

emission, and it is of interest to study the variations of the two emissions at different vertical levels. Comparing their variations with the model provides verifications of the model and allows the vertical transport of atomic oxygen in the model to be examined.

This study compares the global WINDII observations and the TIME-GCM model simulations in order to explore the seasonal climatology of the $O(^1S)$ and OH nightglow emission rates in the mid-to-high latitude region. The study separates the emission variations according to variables of local time and altitude, and depicts a global picture of the emission seasonal variations. The purpose of the study is to distinguish between the different dynamical influences that are responsible for the airglow variations. The major influences considered are the tides and the large-scale mesospheric general circulation; their influences on the emission variations are presented. An additional goal of the study is to understand the underlying mechanism, specifically to what extent vertical motions and eddy diffusion are responsible.

2. WINDII data and the TIME-GCM model

The WINDII instrument and its data processing are extensively described by Shepherd et al. (1993). Airglow emissions from excited atomic oxygen, molecular oxygen, and hydroxyl radicals over altitudes of 80-300 km in the MLT region were regularly observed by WINDII. The nighttime $O(^1S)$ and OH emissions were each observed in a normal schedule of 2 days per week. For each day WINDII measured the volume emission rate profiles in approximately one minute corresponding to about 400 km distance along the satellite orbit. Because of the 57° inclination angle of the orbit and the WINDII pointing direction, the latitudes from 42° in one hemisphere to 72° in the other were alternatively observed for every 36 days during each yaw period, and the range of 42°S-42ºN was continuously observed. The orbit precessed westward at about 5° per day, and the local time covered throughout a single day for a given latitude is about 20 minutes. Because it takes about 36 days for WINDII to cover 24 hrs of local time for a given latitude, the sampling of the diurnal variation of the emission is obtained by composing about one month of the data.

In this study, the WINDII data collected from November 1991 to August 1997 are utilized. WINDII was shut off for some days, causing gaps within the data set. The numbers of days of the observations used for the $O(^1S)$ and OH nighttime emissions for each month through almost 6 years are summarized in Table 1. The number of airglow profiles available for one emission for one night is about 500. Altogether during 1991-1997 there are more than

300,000 and 150,000 WINDII profiles for the $O(^1S)$ and the OH (8-3) band $P_1(3)$ line nightglow emissions, respectively.

To study the seasonal variations, the WINDII level 2 volume emission rate profiles of the nighttime $O(^1S)$ and OH (8-3) band $P_1(3)$ line emissions through 1991-1997 are grouped by month. That is, the observations available for one emission in one month through all the years are combined. For each month, the volume emission rates of one airglow emission at a specific altitude range are further averaged within a bin of 5° in latitude and 2 hrs in local time. The data at the same latitude but different longitudes also at the same local time are averaged. This averaging process largely eliminates the longitudinal variation of the emission rate. Each month of observations covers the whole range of local time, and the monthly averaged results represent the climatological signature of the airglow emission.

The TIME-GCM model developed in NCAR is a three-dimensional model for simulating the global circulation, temperature and compositional structure between 30 and 500 km of the atmosphere (Roble et al., 1987; Roble and Ridley, 1994). It is self-consistent, driven by a time-dependent scheme of coupled thermosphere and ionosphere dynamics and electrodynamics and incorporated with the physical and chemical processes appropriate for the mesosphere and upper stratosphere. The model also incorporates the processes of atomic oxygen production, its transport and loss so is able to simulate the emission rate variations of the oxygen airglow in the MLT region.

For the present study, the TIME-GCM simulations from a recent scheme are utilized which includes daily F10.7 cm solar flux variations and 3 hr Kp variations along with daily NCEP global inputs at the model lower boundary of about 30 km. The model results for the same days of the WINDII observations through the years 1992-1996 are monthly averaged for the purpose of comparison. The volume emission rates of the $O(^1S)$ and OH (8-3) band emissions from the model for the same altitudes, latitudes and local times as WINDII are averaged for each month of the year. This is intended to remove the short-time daily variations and the year-to-year variations, exposing the emission seasonal behavior. It should be noted that the model computes the whole band emission rate of the OH (8-3) emission while the single line emission of $P_1(3)$ from WINDII is employed in the data presentation, roughly ten times smaller. This is not a problem for the study of variation patterns.

Subsequently, the monthly averaged emission rates from the WINDII observations and the TIME-GCM model simulations for the O(^{1}S) and OH nightglow are displayed in a format separating local time and altitudinal effects. The similarities and dissimilarities of the emission variations between WINDII and the TIME-GCM are discussed. The model provides results up to 90º latitude for all seasons, which greatly assists with the interpretations. Diagnostic post-processing on the TIME-GCM output is carried out in order to distinguish the relative importance of vertical motions and eddy mixing.

3. Results

a. Semi-annual and annual variations of the O(^{1}S) emission rate

Figure 1(a) shows the averaged O(^{1}S) volume emission rates observed by WINDII for 96 km altitude and 2 hr local time represented as a function of month of the year and latitude. Four intense emission rate maximums appear from 20º to 40° latitudes in both hemispheres. They occur from mid-April to June and September/October for the northern hemisphere, and in March/April and November/December for the southern hemisphere. A deep emission rate minimum is observed from the end of December to January in the northern hemisphere, and around July/August in the southern hemisphere. In the northern hemisphere the maximums are about 6 months apart, but occur 1-2 months after the equinoxes. In the southern hemisphere the maximums are about 8 months apart across the winter period. The strength of the emission peaks for the two hemispheres is not the same as the maximum emission rate in the northern hemisphere is larger than that in the southern hemisphere by a factor of about 1.1. In the northern hemisphere the spring emission rate maximum is stronger than in autumn, while the maximum is stronger in autumn than in spring for the southern hemisphere; both are strongest in the April/May period. Considering the two hemispheres, it appears that the emission is strong in local spring but delayed by about 2 months with respect to the spring equinox, weakens through the summer, recovers in the fall season, and is largely dissipated in winter. While the emission variation for mid-latitudes appears to be semi-annual, the maximums do not appear just at equinoxes, as they do for the equatorial semi-annual variation.

At an altitude lower by 8 km and a local time later by 2 hr (at 88 km altitude and 4 hr local time), the WINDII O(^{1}S) emission rates shown in Figure 1(b) have a strong autumn maximum near 40º latitude in both hemispheres. The emission peak appears strongly in September/October/November of the local fall season for the northern hemisphere, then

weakens a little during the winter season in December/January/February, and decreases to a minimum during spring and summer from March to August. The same behavior is also evident in the southern hemisphere, with an emission rate maximum in local fall and winter, and a relative minimum in spring and summer. One difference between the two hemispheres is that the emission rate maximum in the southern hemisphere is more extensive than the one in the northern hemisphere, having a longer duration. The southern hemisphere emission minimum occupies a more limited latitude range and has a shorter duration than for the northern hemisphere minimum. Another common signature observed in both hemispheres is that there is a secondary emission rate maximum close to 20° latitude. This minor emission peak is constrained to months around April/May in the northern hemisphere and around October/November in the southern hemisphere, adjacent to the local summer season. In effect, the autumn maximums seen in Figure 1(a) at 96 km for the two hemispheres become stronger and move towards winter for the lower altitude, and at the same time the spring maximums weaken and also move towards winter. At the height of 88 km, the winter emission rates increase and those in summer decrease, creating an annual variation.

Thus the $O(^1S)$ emission appears to be altitude-dependent and it also changes with local time. This is verified by Figure 2, which shows the seasonal variations of the WINDII $O(^1S)$ emission rates within ±40° latitudes for a set of chosen local times and altitudes. At a given altitude and local time for each panel, the volume emission rates are represented as a function of latitude and month of the year. The panels in each row are arranged at successive local times of 20, 22, 24, 02, and 04 hr from the left to the right, and the panels in each column are at decreasing altitudes of 104, 100, 96, 92, 88, and 84 km from the top to the bottom.

The peak of the $O(^1S)$ volume emission rate is observed at about 96 km. For altitudes from 92 to 104 km, the $O(^1S)$ emission mainly portrays a semi-annual variation with four emission rate maximums (two in each hemisphere) at mid-latitudes between ±20º and ±40° similar to Figure 1(a). These semi-annual emission peaks vary with local time, approaching maximum emission rates at midnight or at 02 hr and being relatively weak at dusk. For the lower selected altitudes of 88 and 84 km, the emission rates over mid-latitudes exhibit an annual variation with a maximum in autumn and winter as shown in Figure 1(b). This annual variation also has a local time dependence, yielding large amplitudes at midnight and in the early morning hours but is much weaker in the evening. At the lowest altitude and in the early evening hours the equatorial semi-annual variation becomes dominant.

In contrast, Figure 3(a) shows the TIME-GCM modeled O(^{1}S) emission rates at the altitude of 96 km and local time of 2 hr represented in a latitude versus month-of-year format that is the same as for the WINDII observations. In this figure for the northern hemisphere above 40º latitudes the emission rates include one maximum in November/December and January/February for the local winter season along with another maximum extending from April to August during the local summer between the equinoxes. The emission rates in the southern hemisphere above 40º latitudes also consist of a maximum in winter for May-August and another one in summer for November/December and February/March. It appears that the model sees an annual emission rate variation with a winter maximum and a superimposed summer peak for both hemispheres at mid- and high latitudes. This seasonal variation is asymmetrical with respect to the equator in that the emission rate maximums in the southern hemisphere are about 1.2 times stronger than for the northern hemisphere. The model emission variation resembles more closely the WINDII pattern as shown in Figure 1(b) even though the local time and altitude correspond to Figure 1(a).

The altitude for Figure 3(b) is 12 km lower and the local time 2 hrs later than in Figure 3(a). Despite the differences, the model sees a similar local winter emission rate maximum at latitudes above 40º in both hemispheres. For 84 km altitude and 4 hr local time, the maximum occurs in November/December and extends into January in the northern hemisphere, and appears in June/July/August in the southern hemisphere. The southern hemisphere winter maximum is about 2 times stronger than the one in the northern hemisphere. The maximums create a pronounced annual variation for the mid- and high latitude ranges of both hemispheres since the summer peaks have vanished. This modeled annual variation is also very similar to that of the WINDII observations shown in Figure 1(b), but is delayed by about 2 months.

Figure 4 shows the TIME-GCM emission rates of the O(^{1}S) emission for the set of chosen altitudes and local times from 84 to 104 km and from 20 to 04 hr with the latitudes extending to 90°. The model emission patterns for the same altitude but different local times are almost the same, although the emission rates are somewhat larger in the early morning than in the evening. At the lowest altitude the model results feature an annual variation having a winter emission rate maximum above 40º latitudes in both hemispheres. At higher altitudes from 88 to 100 km a summer emission rate maximum is superimposed on this annual variation. The

summer peaks occur from late May to late August for the northern hemisphere and around January/February and November/December for the southern hemisphere, shortly before or after the emission rate minimums at the equinoxes. They are slightly weaker than the winter maximums for altitudes of 88 and 100 km, almost disappear at 104 km, but get stronger at the peak altitudes of the emission around 96 km. On the whole, compared with the WINDII observations in Figure 2, the model results in the mid-to-high latitude region are quite similar to the low altitude emission data but are delayed by few months. The semi-annual variation for the higher altitudes in the WINDII data is not seen by the TIME-GCM.

b. Annual variation and summer maximum of the OH emission rate

Figure 5(a) shows the WINDII observed emission rates at an altitude of 80 km and a local time of 4 hr for the OH (8-3) band $P_1(3)$ line emission represented as a function of month of the year and latitude. An annual variation is evident at this altitude and local time showing a winter emission rate maximum near 40° latitude in each of the two hemispheres. The winter emission peak occurs for the months of November-February in the northern hemisphere, and for April-August in the southern hemisphere. It is stronger in the southern hemisphere than in the northern hemisphere by a factor of about 1.5. In addition, a secondary emission peak appears for limited latitudes of around 30° in the northern hemisphere around June/July in the local mid-summer, but is absent in the southern hemisphere. Another distinct signature of the emission variation at this altitude is that the equatorial semi-annual variation stands out. This semiannual variation at the equator has a larger maximum in March/April than in September/October.

The extra-tropical summer maximum extends from 20º to 40º latitude in each hemisphere and is much stronger at the higher altitude and earlier local time as shown in Figure 5(b), which displays the OH emission rates from the WINDII observations for 88 km altitude and 22 hr local time. For this altitude and local time, the emission variation reveals a clear summer peak for June/July in the northern hemisphere and for December/January in the southern hemisphere, occurring in the local mid-summer of both hemispheres. The variation pattern in Figure 5(b) for the mid-latitude region is almost the reverse of Figure 5(a), showing an annual variation with the maximum occurring in summer rather than in winter. The equatorial semi-annual variation in Figure 5(b) is very clear, but the two maximums have the same emission rate, unlike Figure 5(a).

Figure 6 displays the collection of seasonal variations of the WINDII observed volume emission rates of the OH (8-3) Meinel band $P_1(3)$ line emission for the selected altitudes and local times from 100 km to 80 km and from 20 hr to 04 hr. The emission rates at mid-latitudes exhibit a variation pattern depending on altitude as well as on local time. The height of the OH emission peak is at 88 km, and the emission rate decreases above or below this height. For altitudes of 80 and 84 km an annual variation as seen in Figure 5(a) is observed having a strong emission maximum in winter near 40º latitudes in both hemispheres. This annual variation is strongest in the early morning hours but almost disappears for the early night at 20 hr and 22 hr local time. A summer emission maximum as seen in Figure 5(b) is evident around ±40° latitudes in each of the two hemispheres for altitudes of 88 and 92 km. The summer peak is also observed at 84 km for the northern hemisphere, but disappears for the southern hemisphere. For altitudes of 88 km and higher the emission includes four regions of large emission rates at ±40° latitudes, creating a semi-annual variation in each of the two hemispheres. These emission rates also change with local time, being strongest in the early morning hours but largely dissipated in the evening.

In comparison, Figure 7(a) shows the TIME-GCM model emission rates for the OH (8-3) band emission at the altitude of 80 km and local time of 4 hr represented as a function of month of the year and latitude. As for the WINDII observations for the same altitude and local time in Figure 5(a), the model reproduces an annual variation around 60º latitudes in both hemispheres. The model emission features a pronounced emission rate maximum during November-February for the northern hemisphere and in April-August for the southern hemisphere, during local winter season of the two hemispheres. For the higher altitude of 88 km and the earlier local time of 22 hr shown in Figure 7(b), the TIME-GCM model simulates four emission rate maximums between ±40º and ±90° in two hemispheres. These emission peaks occur in February/March and November/December for the northern hemisphere and in May/June and August/September for the southern hemisphere. They are adjacent to equinoxes for both hemispheres, rather creating a semi-annual variation for the mid-to-high latitude region. Another feature of the model OH emission is that there are superimposed summer peaks at ±40°-±60° latitudes. They are located in May-September for the northern hemisphere and in November-February for the southern hemisphere, in the local summer season of the two hemispheres. The summer peak signature is quite similar to the WINDII data for the same altitude and local time as shown in Figure 5(b).

Similarly, Figure 8 displays the TIME-GCM model results of the seasonal variations of the OH (8-3) band emission for the sequence of altitudes from 80 to 100 km and local times from 20 to 4 hr. The model emission rate patterns are near symmetric on a seasonal basis between the two hemispheres for each altitude and local time. At the altitudes of 80 and 84 km, the TIME-GCM emission shows a prominent annual variation with a strong emission rate maximum in winter and a deep minimum in summer between 40° and 90° latitudes for both hemispheres. This variation in the model persists throughout the whole night, being relatively stronger in the evening than in the early morning, but the annual pattern in WINDII is observed only at midnight and in the morning hours. At 88 km and 92 km altitudes, the TIME-GCM simulates a remarkable emission maximum for local summer around ±40° latitude in each of the two hemispheres, which is also observed by WINDII. The summertime mid-latitude maximum extends to 84 km where the signature is less recognizable. At the altitudes of 92, 96 and 100 km around ±60° latitudes, the TIME-GCM results include four relatively intense emission rate maximums close to equinoxes for both hemispheres, corresponding to a semi-annual variation that is not so strong in the WINDII data. The model emission variation varies with local time, being strongest in the evening specifically for 96 and 100 km altitudes. The equatorial semi-annual variation is very strong in the model for the lower altitudes of 80-88 km, reaching its maximum amplitude around mid-night or in the early morning. The model variation for OH is rather similar to that of the WINDII data for the $O(^1S)$ emission.

4. Summary and Discussion

There are many similarities between the TIME-GCM model results and the WINDII observations for the $O(^1S)$ and OH nightglow seasonal variations. Both WINDII and the model exhibit a similar variation pattern of the airglow emission rate in the mid-to-high latitude regions of the two hemispheres. Both show that the presence of the annual and semi-annual variations depends strongly on the altitude level and local time. Below 88 km, both the $O(^1S)$ and OH emissions mainly have an annual variation with an emission rate maximum in the fall or winter season. Above this height, a semi-annual pattern with emission rate maximums close to equinoxes is the prominent feature in the WINDII data for the $O(^1S)$ emission and in the TIME-GCM simulations for the OH emission. In addition, both WINDII and the model include a superimposed summer peak for the OH emission at 88 km altitude.

The annual variation in the mid-to-high latitude region with an emission rate minimum in summer and a maximum in winter is evident in the TIME-GCM model results for the $O(^1S)$ and OH emissions below 88 km throughout the whole night. The WINDII data also show the annual variation for these emissions at these heights but mostly for midnight and early morning hours. The annual variation in the model for the $O(^1S)$ emission extends to higher altitudes, where it is not observed by WINDII. The mid-to-high latitude semi-annual variation is seen by the TIME-GCM and WINDII, but the TIME-GCM sees it only in the OH emission and WINDII observes it most obviously for the $O(^1S)$ emission. This semi-annual variation is revealed by the model OH emission over the altitude range from 92 to 100 km, and it is observed in the WINDII $O(^1S)$ emission through 92-104 km. WINDII strongly observes the semi-annual variation around midnight and in the early morning hours, while the TIME-GCM sees the strongest variation in the evening hours. Thus the same patterns are seen in the emission rate variations by both WINDII and the TIME-GCM, but the altitude and local time regimes do not exactly correspond. The model variation patterns occur a few hours earlier than in the WINDII data, and they appear to be about 8 km higher than the observed variations.

The apparent semi-annual variation in the $O(^1S)$ emission was observed by the OGO-6 and ISIS-II satellite instruments (e.g. Donahue et al., 1973; Cogger et al., 1981), respectively. As for WINDII, the maximums of emission rates were not exactly located at the equinoxes. The emission annual variation is dominant at high latitudes as observed by ground-based instruments (e.g. Deutsch and Hernandez, 2003), having an emission rate minimum in spring and a maximum in autumn. In other words, the earlier satellite observations correspond most closely to the higher-altitude WINDII observations, while the ground-based observations correspond better to the lower-altitude observations. It is not clear why the satellite and ground-based results should be so different, but local time may be involved. The mid-summer peak reported here is seen in the ground-based data presented by Deutsch and Hernandez (2003) but was not noted in the earlier satellite data.

The mechanism for the emission semi-annual and annual variation at mid-to-high latitudes has yet to be discussed. In the context of dynamics, tides and the large-scale general circulation appear to be the major influences. In terms of processes, vertical motions and eddy diffusion both operate to transport atomic oxygen from the region where it is created to the lower levels where the density levels are high enough to maintain the airglow. Because of

the agreement between the WINDII observations and the TIME-GCM simulations, it is possible to use the model for diagnostic purposes.

As noted earlier, it has been established that the diurnal tide at the equator is responsible for the dramatic airglow emission rate variations there (e.g. Takahashi et al., 1995; Burrage et al., 1995; Angelats I Coll and Forbes, 1998; Ward, 1999; Roble and Shepherd, 1997; Marsh et al., 2006). The diurnal tide enhances the O(^{1}S) emission at the equator in the early evening but the emission enhancement divides and moves away from the equator, reaching 40° latitude in the early morning (e.g. Shepherd, et al., 1998; Zhang et al., 2001). This can also be seen in Figure 2, in the panels for 92 km altitude. Since the diurnal tide has a semi-annual behavior this variation is then imparted to the mid-latitude airglow. This happens only at higher altitudes, in the region where the diurnal tide dissipates. The semi-annual variation is not seen at lower altitudes for the O(^{1}S) emission and not at all for the OH emission. The tidal influence on the variations of the oxygen airglow emissions and the relative importance of vertical winds and eddy diffusion on the transport of atomic oxygen are now assessed.

The upward/downward fluxes of atomic oxygen, the numbers of oxygen atoms flowing through a unit horizontal area during a unit time (in units of m^{-2} second^{-1}), due to the two processes of vertical winds and eddy diffusion are calculated from the TIME-GCM model results. For vertical winds, the fluxes (*f*) are obtained by multiplying the wind velocities (*w)* by the atomic oxygen number densities (N_O) as expressed as: $f = W \times N_O$. For eddy diffusion, the flux of atomic oxygen is equal to: $f = K \times N \times \frac{d}{dZ}(\frac{N_O}{N})$, where *K* is the eddy diffusion coefficient, *Z* denotes the vertical coordinate, *N* is the number density of the atmosphere, and N_O/N is the atomic oxygen mixing ratio. Figures 9 and 10 show the calculated atomic oxygen fluxes corresponding to vertical advection and eddy mixing, respectively. As shown in Figure 10, eddy diffusion for the altitudes of 80-100 km is always downward for almost all local times and the amplitude of the atomic oxygen flux is rather consistent throughout a day. The flux from vertical winds in Figure 9 is a factor-of-ten larger at certain local times and changes its direction during a day. The variation of the flux has a diurnal pattern for the equator but is semi-diurnal at the mid-latitude band. Therefore, eddy diffusion contributes to the background airglow while vertical wind associated with the tides

explains the local time variation in the atomic oxygen transport and the oxygen airglow emission rate. This appears to be as true at mid-latitudes as it is at the equator.

As seen in both the WINDII data and the TIME-GCM model results, the annual variation of the $O(^1S)$ and OH emissions at mid-to-high latitudes has a winter emission rate maximum and a summer minimum. This is almost certainly the result of the mesospheric general circulation, as further shown in Figure 11 which presents the daily mean values of atomic oxygen fluxes through the transport of vertical winds and eddy diffusion based on the TIME-GCM model results. The figure shows that at the altitude levels of 80-95 km the transport of atomic oxygen is downward for both winter and summer, but the total atomic oxygen flux is almost 10 times larger in winter than in summer. The downward transport brings atomic oxygen from its origin to the levels where the oxygen airglow emission occurs, but the transport in winter is much stronger and brings down more atomic oxygen producing a larger emission rate of the airglow.

From the results shown earlier the annual emission variation is observed only at lower altitudes and the influence of the large-scale general circulation on the emission variation appears more clearly in the mesosphere than in the lower thermosphere. Pan et al. (2002) showed that the meridional flow may not extend to such as high altitudes as previously thought, consistent with what is shown here. Both WINDII and the TIME-GCM see a secondary summer emission peak for the OH emission at 88 km altitude, and the overall summer minimum of the annual variation is partially filled in with a maximum. The summer emission peak has been reported from the ground-based observations in previous studies (Hecht et al., 1997; Espy and Stegman, 2002), but its mechanism has not been identified. As also shown in Figure 11, the atomic oxygen flux for summer at 88 km from eddy diffusion is about 2 times larger than that from vertical advection. This suggests that enhanced eddy diffusion could be responsible for the summertime OH emission maximum.

5. Conclusions

This study depicts the seasonal variations of the $O(^1S)$ and OH airglow emissions at mid-to-high latitudes for various altitudes and local times from the WINDII observations. The purpose of the study is to understand the airglow variability from the perspective of vertical transport of atomic oxygen in the MLT region. To interpret the observed emission variation signatures, the WINDII data are inter-compared with the simulations of the TIME-GCM

model. In general, the model produces similar emission variations as observed in the real data, suggesting that the mechanisms employed in the model are responsible for what is seen in the data. The investigation results for the seasonal variations of the oxygen airglow emission rates at mid-to-high latitudes are summarized as follows.

1. The semi-annual and annual variations occur together but for different altitudes and specific local times. The semi-annual variation exists at higher altitudes, while the annual variation is mostly seen at lower altitudes. Their altitude and local time regimes do not exactly correspond between WINDII and the TIME-GCM. The WINDII $O(^1S)$ variation at high altitude corresponds best to the OH variation predicted by the model.

2. The emission semi-annual variation appears to be coherent with tidal activity. Some of the variation in atomic oxygen density and airglow emission rate could be explained by vertical winds associated with the tides. Vertical advection plays a relatively more important role than eddy diffusion for the local time variation.

3. The annual variation of the airglow emission rate is the result of the mesospheric general circulation. The winter maximum of the emission rate corresponds to a stronger downward transport of atomic oxygen. The influence of the large-scale circulation appears more clearly in the mesosphere than in the lower thermosphere.

4. The overall summer emission rate minimum of the annual variation is partially filled in with a summer peak, which is mainly shown for the OH emission at 88 km altitude. The summer peak could be caused by enhanced eddy diffusion.

These results have described in some detail the influence of the large-scale circulation and identified other processes in the seasonal variation of airglow emission rate that require further study.

Acknowledgments

The WINDII project is a collaboration between the Canadian Space Agency and the Centre National d'Etudes Spatiales of France, with the mission support provided by NASA. The scientific analysis of the data is supported by the National Research Council of Canada. The National Center for Atmospheric Research is sponsored by the National Science Foundation.

References

Andrews, D. G., J. R. Holton, and C. B. Leovy (1987), Middle atmosphere dynamics, *Academic Press,* Orlando, Florida.

Angelats I Coll, and Forbes (1998), Dynamical influence on atomic oxygen and 5577 Å emission rates in the lower thermospehre, *Geophys. Res. Lett., 25*, 461-464.

Brasseur, G., and S. Solomon (1986), Aeronomy of the Middle Atmosphere, *D. Reidel Publishing Co.*, Dordrecht, Holland.

Burrage, M. D., M. E. Hagan, W. R. Skinner, D. L. Wu, and P. B. Hays (1995), Long-term variability in the solar diurnal tide observed by HRDI and simulated by the GSWM, *Geophys. Res. Lett.*, *22*, 2641-2644.

Cogger, L. L., R. D. Elphinstone, and J. S. Murphree (1981), Temporal and latitudinal 5577Å airglow variations, *Can. J. Phys.*, *59*, 1296-1307.

Deutsch, K. A., and G. Hernandez (2003), Long-term behavior of the OI 558 nm emission in the night sky and its aeronomical implications, *J. Geophys. Res., 108*, 1430-1447, doi: 10.1029/2002JA009611.

Donahue, T., M., B. Guenther, and R. J. Thomas (1973), Distribution of atomic oxygen in upper-atmosphere deduced from OGO 6 airglow, *J. Geophys. Res., 78*, 6662-6689.

Espy, P. J., and J. Stegman (2002), Trends and variability of mesospheric temperature at high-latitudes, *Phys. Chem. Earth*, *27*, 543-553.

Fukuyama, K. (1977), Airglow variations and dynamics in the lower thermosphere and upper mesosphere - II: Seasonal and long-term variations, *J. Atmos. Terr. Phys.*, *39*, 1-14.

Garcia, R. R., and S. Solomon (1985), The effect of breaking gravity waves on the dynamics and chemical composition of the mesosphere and lower thermosphere, *J. Geophys. Res.*, *90*, 3850-3868.

Hecht, J. H., R. L. Walterscheid, J. Woithe, L. Campbell, R. A. Vincent, and I. M. Reid (1997), Trends of airglow imager observations near Adelaide, Australia, *Geophys. Res. Lett.*, *24*, 587-590.

Liu, H. L., and R. G. Roble (2004), Dynamical processes related to the atomic oxygen equinox transitions, *J. Atmos. Solar-Terr. Phys., 66*, 769-779.

Makhlouf, U. B., R. H. Picard, M. J. Taylor, and J. R. Winick (1997), Gravity waves and vertical diffusion in the lower thermosphere from 557.7 nm airglow, *Adv. Space Res.*, *19*, 583-586.

Marsh, D. R., A. K. Smith, M. G. Mlynczak, and J. M. Russell III (2006), SABER observations of the OH Meinel airglow variability near the mesopause, *J. Geophys. Res.*, *111,* A10S05, doi:10.1029/2005JA011451.

McDade, I. C., and E. J. Llewellyn (1986), The excitation of $O(^1S)$ and O_2 bands in the nightglow: a brief review and preview, *Can. J. Phys.*, *64,* 1626-1630.

McDade, I. C., E. J. Llewellyn, D. P. Murtagh, R. G. H. Greer (1987), ETON 5: Simultaneous rocket measurements of the OH Meinel $\Delta v=2$ sequence and (8,3) band emission profiles in the nightglow, *Planet. Space Sci.*, *35*, 1137-1147.

McLandress, C., G. G. Shepherd, and B. H. Solheim (1996), Satellite observations of thermospheric tides: results from the wind imaging interferometer on UARS, *J. Geophys. Res., 101*, 4093-4114.

Meriwether, J. W. (1989), A review of the photochemistry of selected nightglow emissions from the mesopause, *J. Geophys. Res.*, *94*, 14,629-14,646.

Pan, W., C. S. Gardner, and R. G. Roble (2002), The temperature structure of the winter atmosphere at South Pole, *Geophys. Res. Lett.*, *29*, doi:10.1029/2002GL015288.

Rayleigh, Lord (Strutt, R. J.) (1928), The light of the night sky: its intensity variations when analyzed by colour filters, III, *Proc. Roy. Soc. (London)*, *A119,* 11-33.

Roble, R. G., E. C. Ridley, and R. E. Dickinson (1987), On the global mean structure of the thermosphere, *J. Geophys. Res.*, *92,* 8745-8758.

Roble, R. G., and E. C. Ridley (1994), A thermosphere/ionosphere/mesosphere electrodynamics general circulation model (TIME-GCM): equinox solar cycle minimum simulations (30-500 km), *Geophys. Res. Lett.*, *21*, 417-420.

Roble, R. G., and G. G. Shepherd (1997), An analysis of Wind Imaging Interferometer observations of $O(^1S)$ equatorial emission rates using the thermosphere/ionosphere/ mesosphere electrodynamics general circulation model, *J. Geophys. Res.*, *102*, 2467-2474.

Shepherd, G. G., et al. (1993), WINDII, the wind imaging interferometer on the Upper Atmosphere Research Satellite, *J. Geophys. Res.*, *98*, 10,725-10,750.

Shepherd, G. G., C. McLandress, and B. H. Solheim (1995), Tidal influence on $O(^1S)$ airglow emission rate distributions at the geographic equator as observed by WINDII, *Geophys. Res. Lett.*, *22*, 275-278.

Shepherd, G. G, R. G. Roble, S. Zhang, C. McLandress, and R. H. Wiens (1998), Tidal influence on midlatitude airglow: comparison of satellite and ground-based observations with TIME-GCM predictions, *J. Geophys. Res.*, *103*, 14,741-14,751.

Shepherd, G. G., G. Liu, and R. G. Roble (2005), Large-scale circulation of atomic oxygen in the upper mesosphere and lower thermosphere, *Adv. Space Res.*, *35*, 1945-1950.

Taylor, M. J., D. C. Fritts, and J. R. Isler (1995), Determination of horizontal and vertical structure of an unusual pattern of short period gravity waves imaged during ALOHA-93, *Geophys. Res. Lett.*, *22*, 2837-2840.

Takahashi, H., B. R. Clemesha, and P. P. Batista (1995), Predominant semi-annual oscillation of the upper mesospheric airglow intensities and temperatures in the equatorial region, *J. Atmos. Terr. Phys.*, *57*(4), 407-414.

Ward, W. E. (1999), A simple model of diurnal variations in the mesospheric oxygen nightglow, *Geophys. Res. Lett., 26*, 3565-3568.

Yee., J. H., R. G. Roble, W. R. Skinner, M. D. Burrage, and P. B. Hays (1997), Global simulations and observations of $O(^1S)$, $O_2(b^1\sum_g^+)$ and OH mesospheric nightglow emission, *J. Geophys. Res.*, *102,* 19,949-19,968.

Zhang, S. P., R. G. Roble, and G. G. Shepherd (2001), Tidal influence on the oxygen and hydroxyl nightglows: Wind Imaging Interferometer observations and thermosphere/iononsphere/mesosphere electrodynamics general circulation model, *J. Geophys. Res., 106*, 21,381-21,393.

Figures:

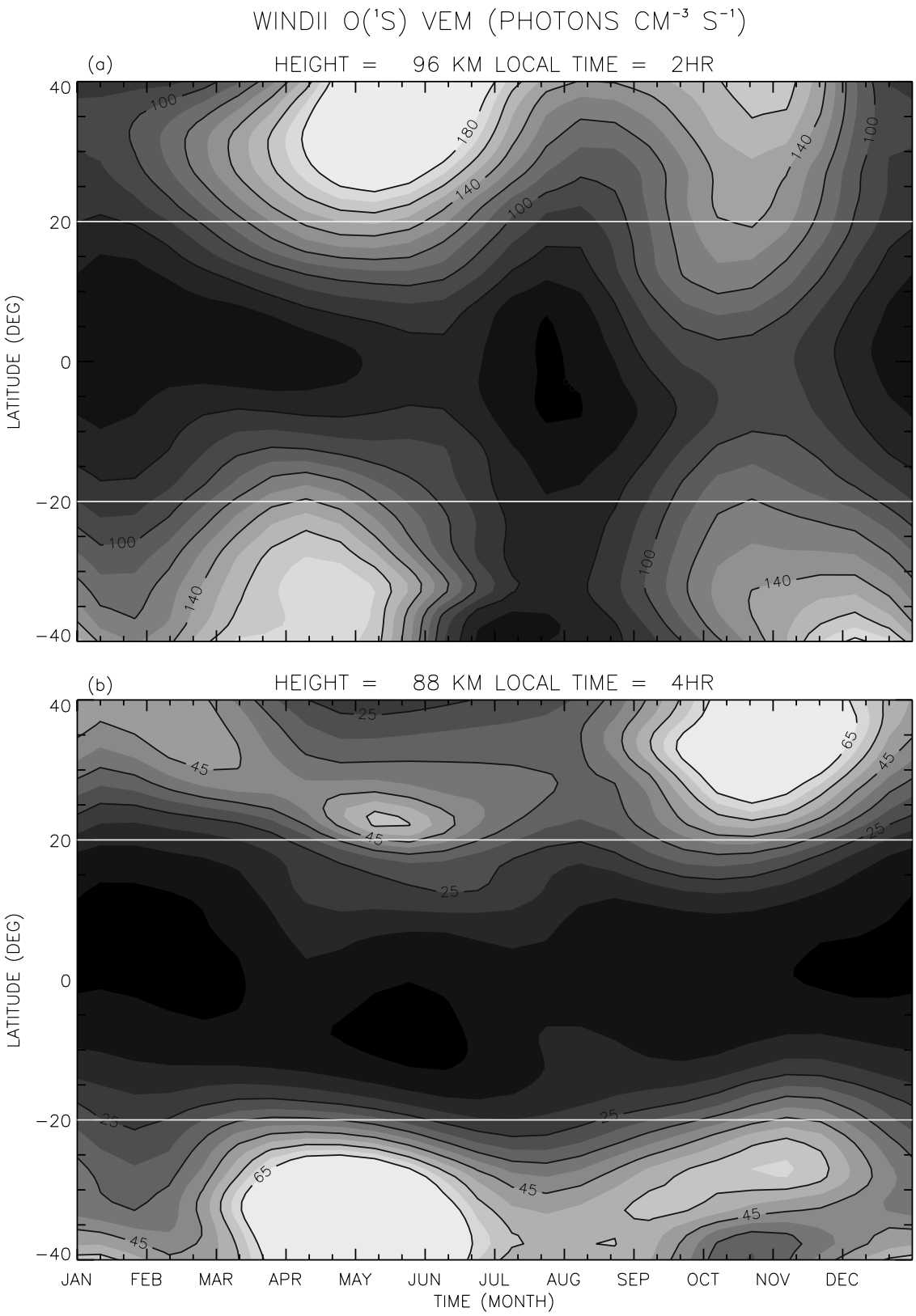

Figure 1: The seasonal variations of the O(^{1}S) nightglow volume emission rates observed by WINDII for (a) 96 km altitude and 2 hr local time, and (b) 88 km and 4 hr local time. The white lines separate the latitude regions of the tropics and the extra-tropics.

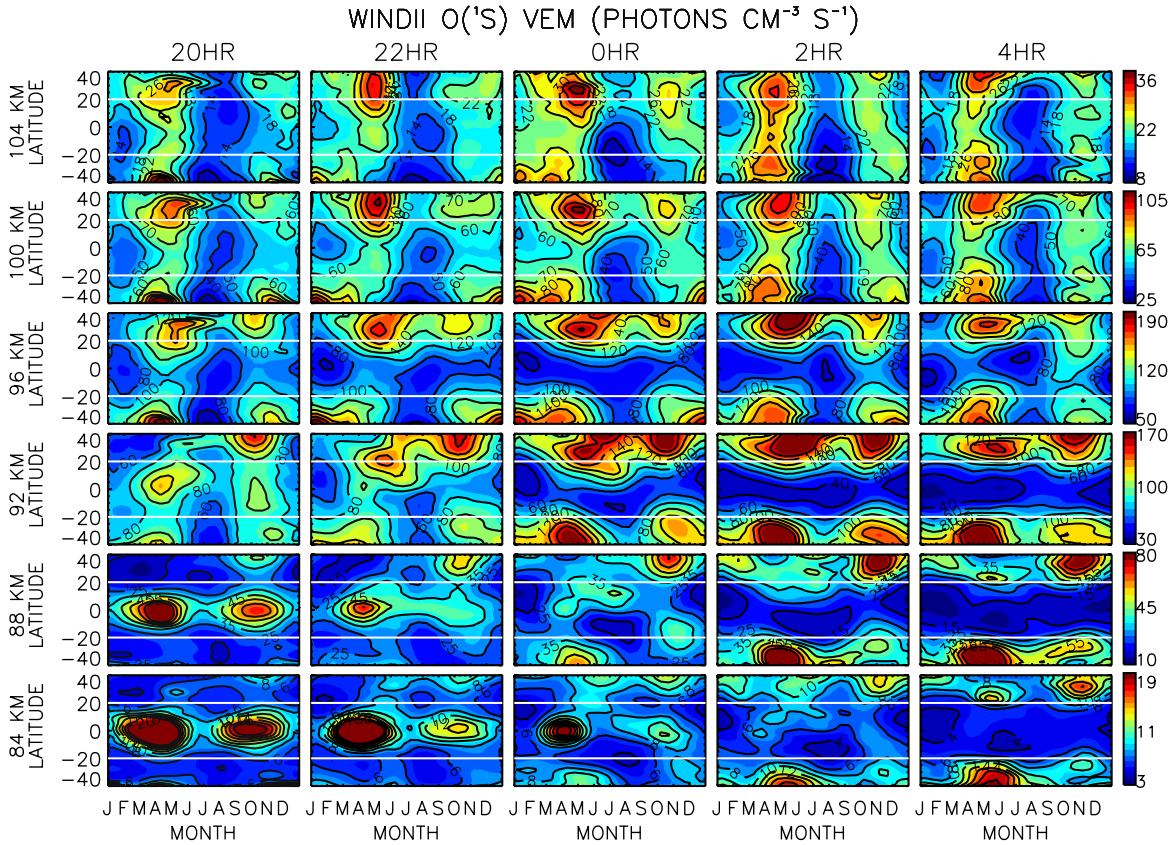

Figure 2: Seasonal variations of the O(^{1}S) nightglow volume emission rates as observed by WINDII for altitudes from 104 to 84 km (panels from the top to the bottom) and local times from 20 to 04 hr (panels from the left to the right). The superimposed white lines separate the tropics and the extra-tropics.

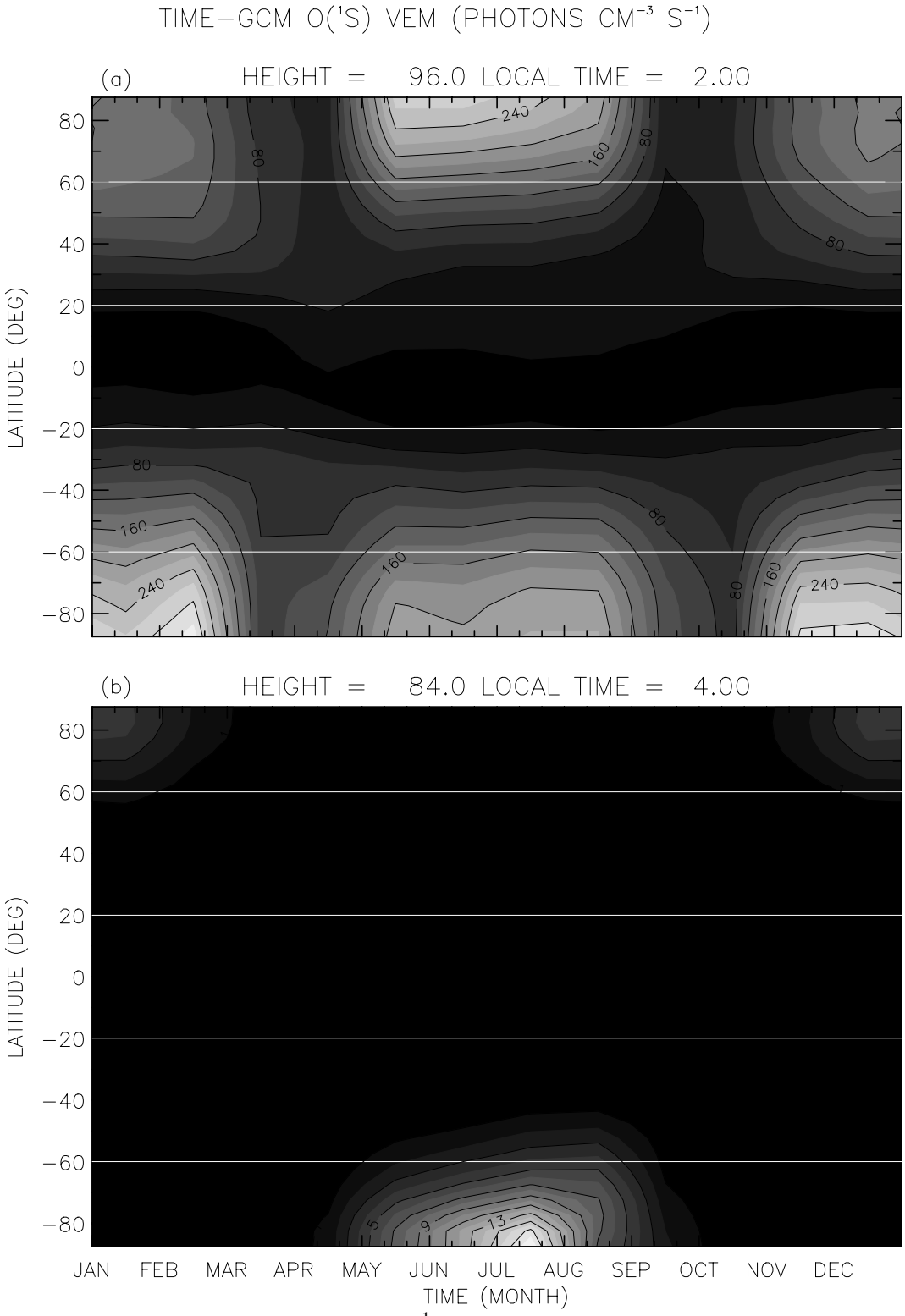

Figure 3: Seasonal variations of the O(^{1}S) nightglow volume emission rates simulated with the TIME-GCM model for (a) 96 km altitude and 2 hr local time, and (b) 84 km and 4 hr local time.

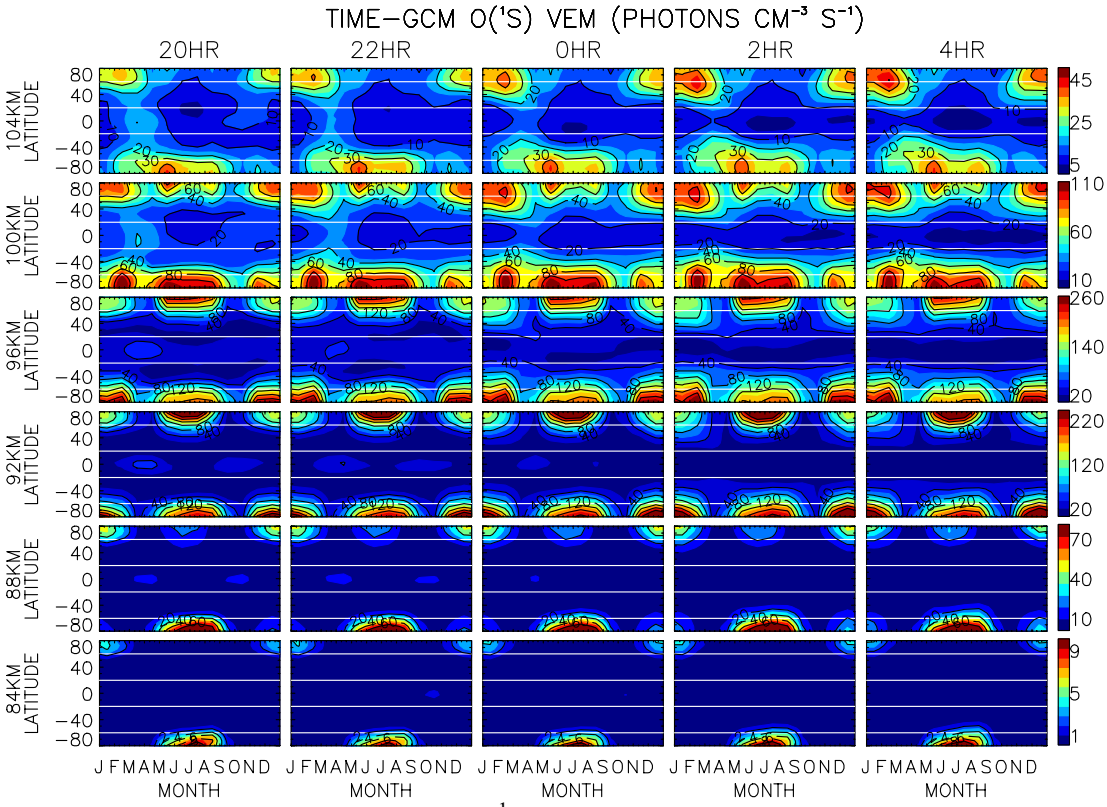

Figure 4: Seasonal variations of the O(^{1}S) nightglow volume emission rates as simulated with the TIME-GCM model for altitudes of 104-84 km and local times of 20-04 hr.

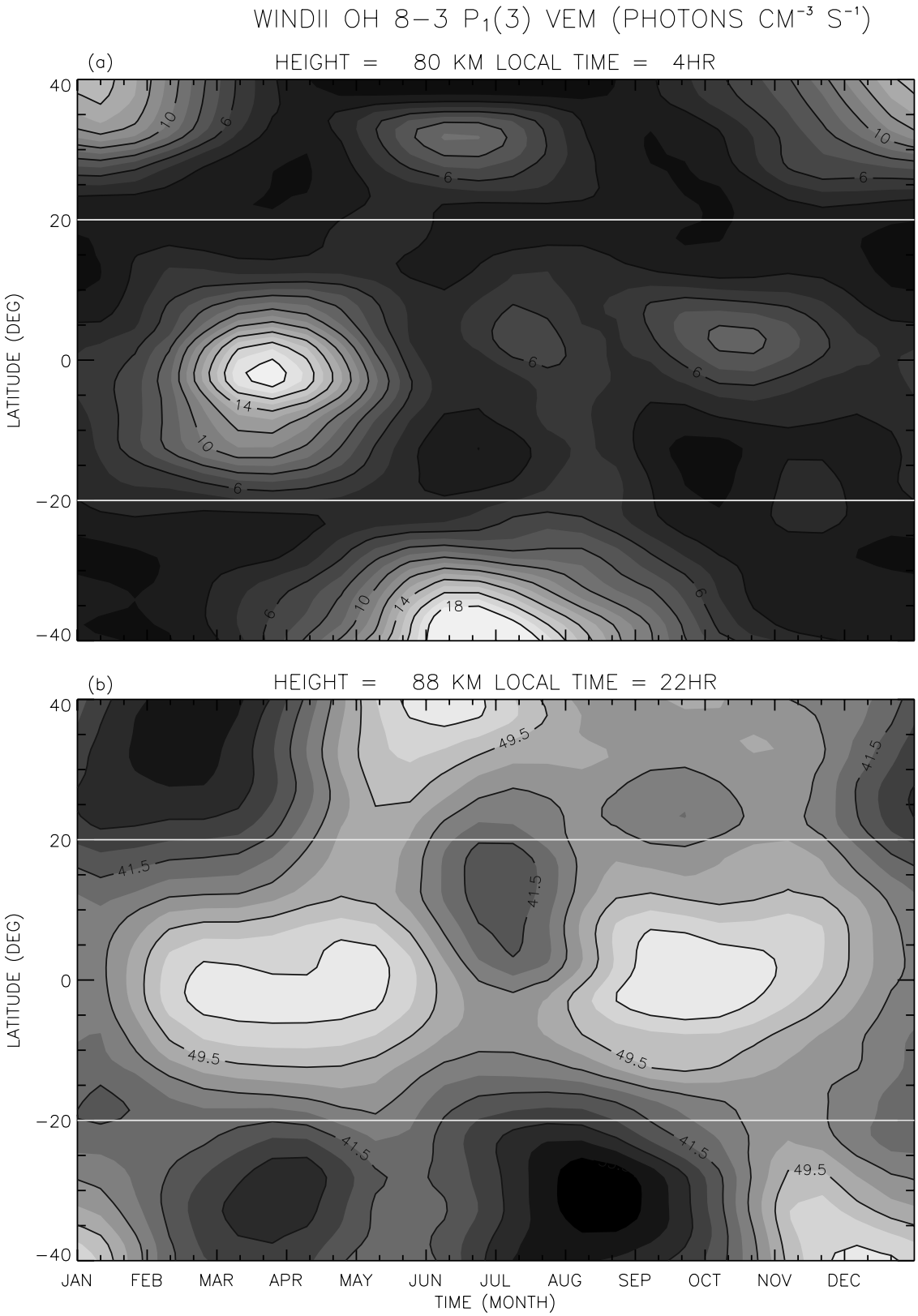

Figure 5: Seasonal variations of the OH (8-3) band $P_1(3)$ line volume emission rates observed by WINDII for (a) 80 km altitude and 4 hr local time, and (b) 88 km and 22 hr local time.

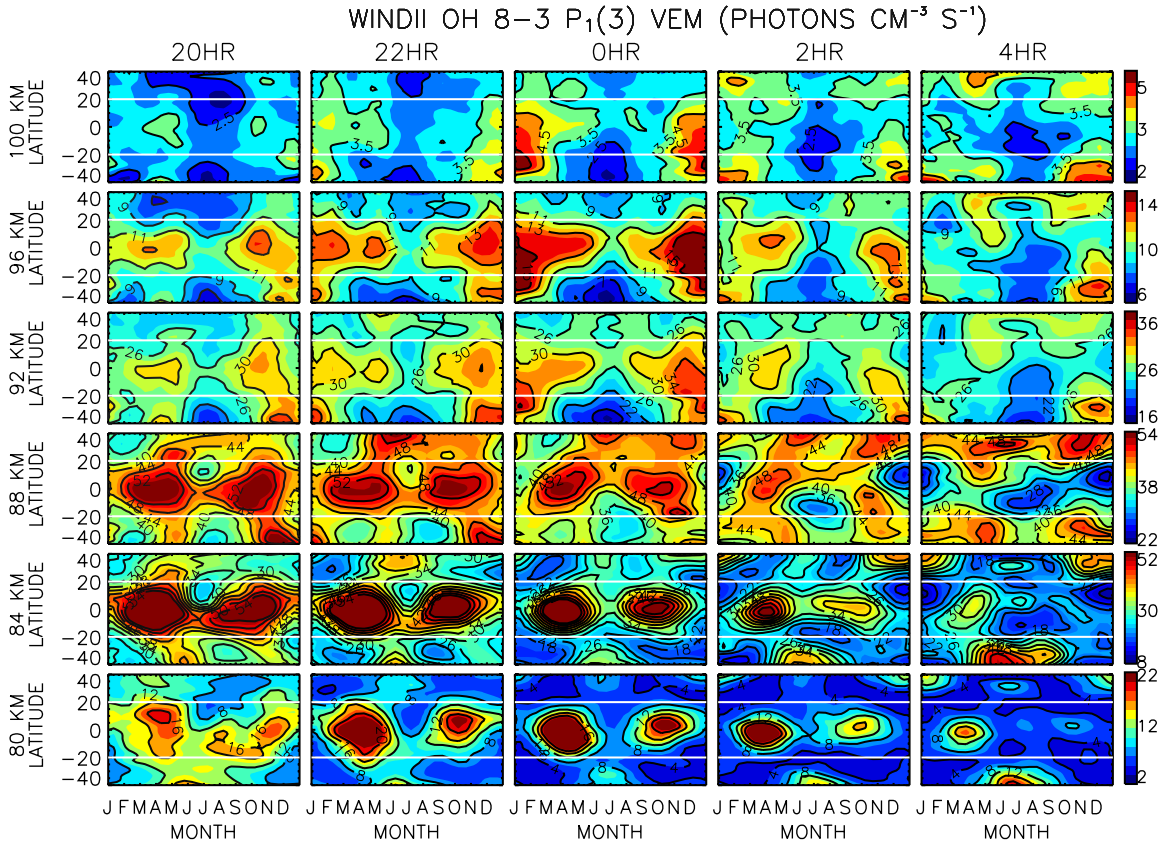

Figure 6: Seasonal variations of the OH (8-3) band $P_1(3)$ line volume emission rates as observed by WINDII for altitudes of 100-80 km and local times of 20-04 hr.

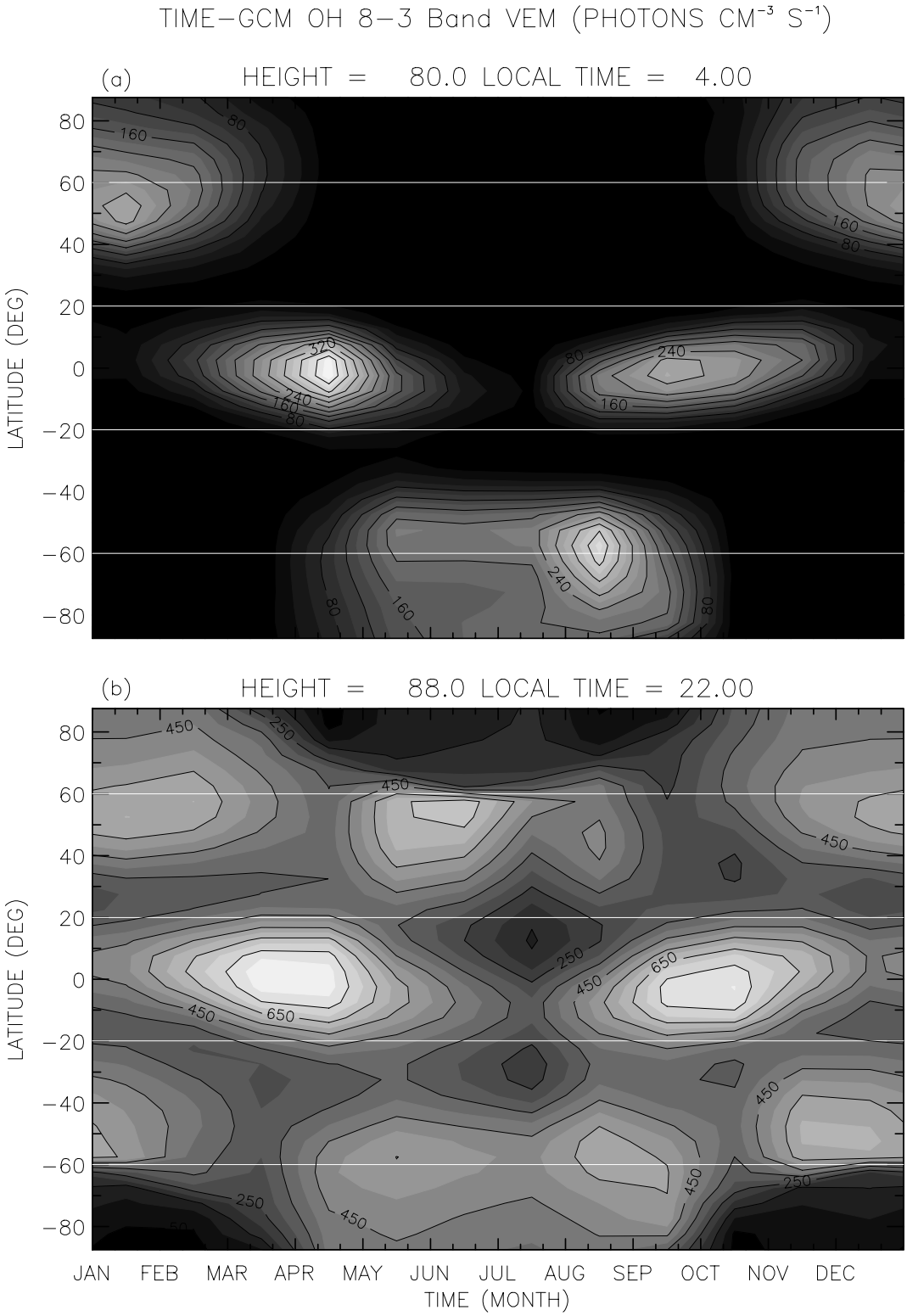

Figure 7: Seasonal variations of the OH (8-3) band volume emission rates as simulated with the TIME-GCM model for (a) 80 km altitude and 4 hr local time, and (b) 88 km altitude and 22 hr local time.

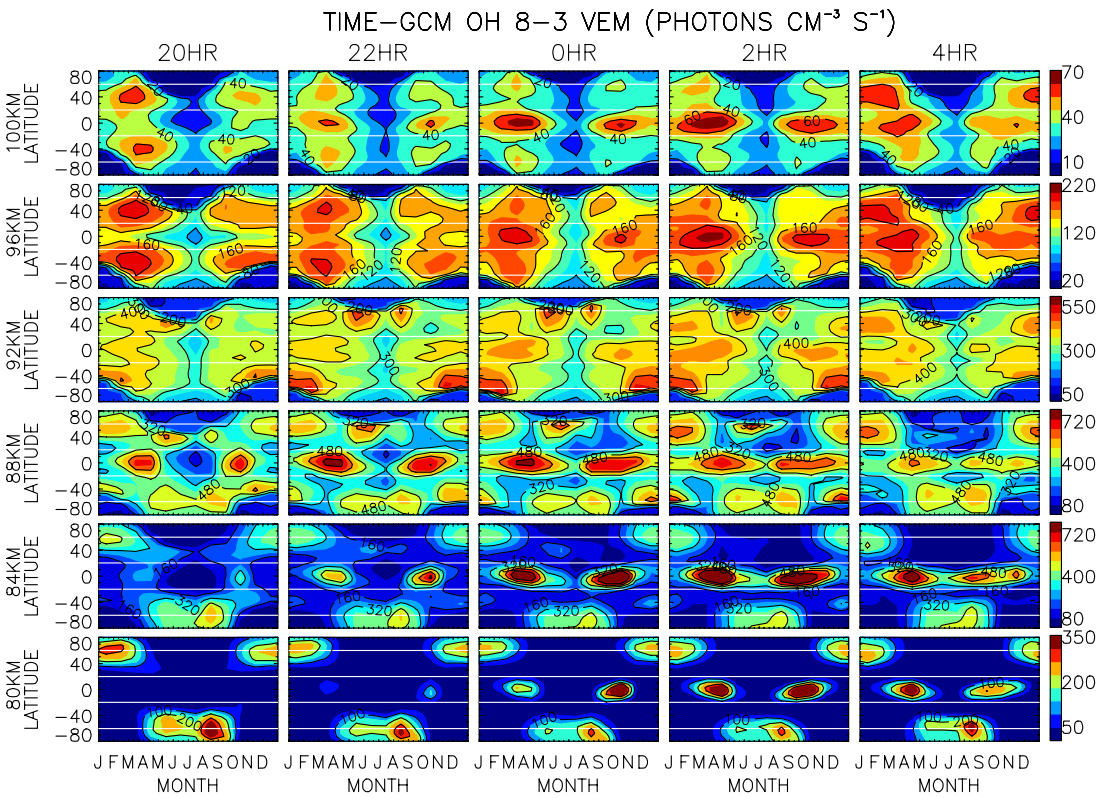

Figure 8: Seasonal variations of the OH (8-3) band volume emission rates as simulated with the TIME-GCM model for altitudes of 100-80 km and local times of 20-04 hr.

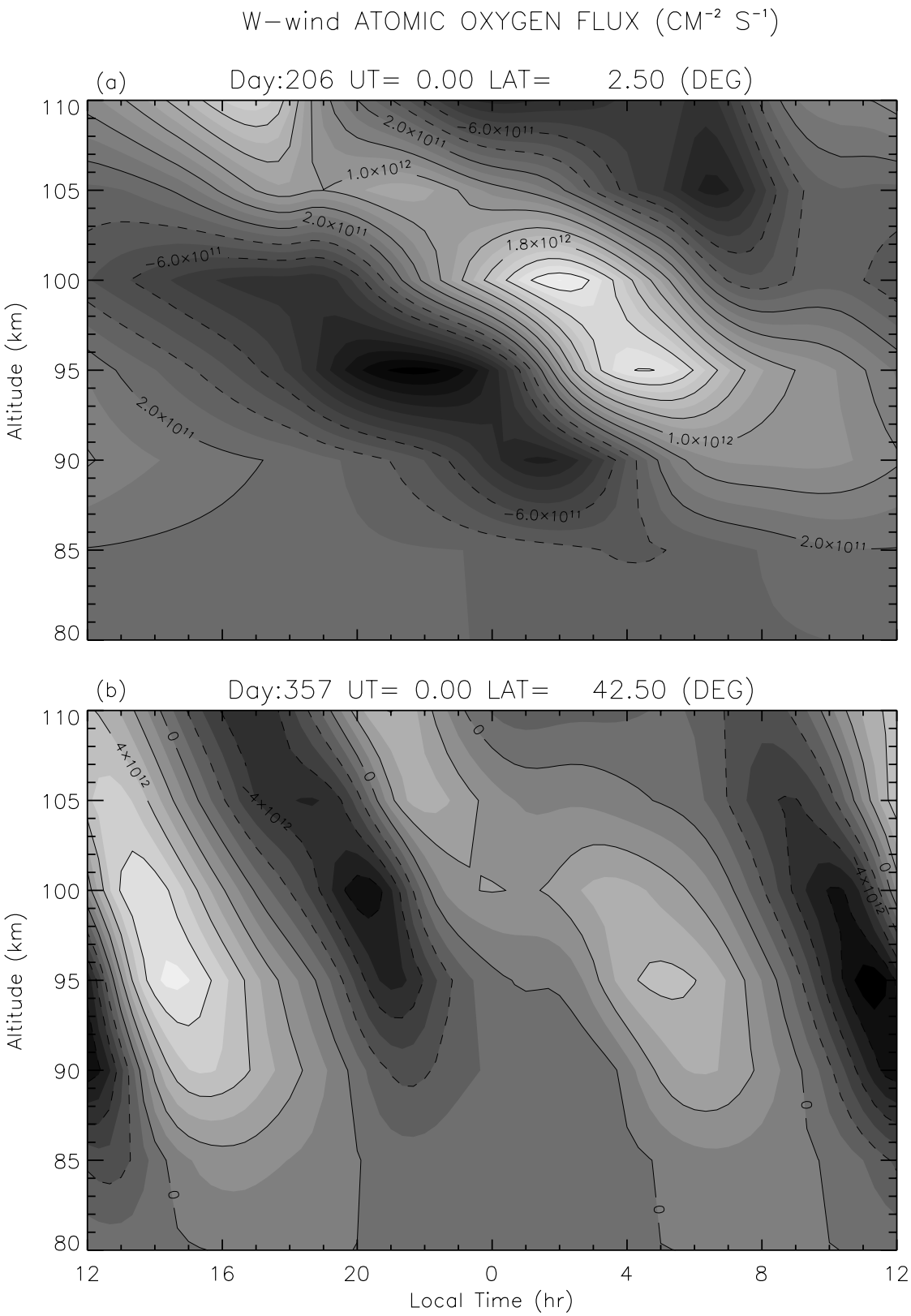

Figure 9: Atomic oxygen fluxes transported by vertical winds as from the TIME-GCM simulations for (a) 2.5º latitude on July 24, 1992, and for (b) 42.5º latitude on December 22, 1992.

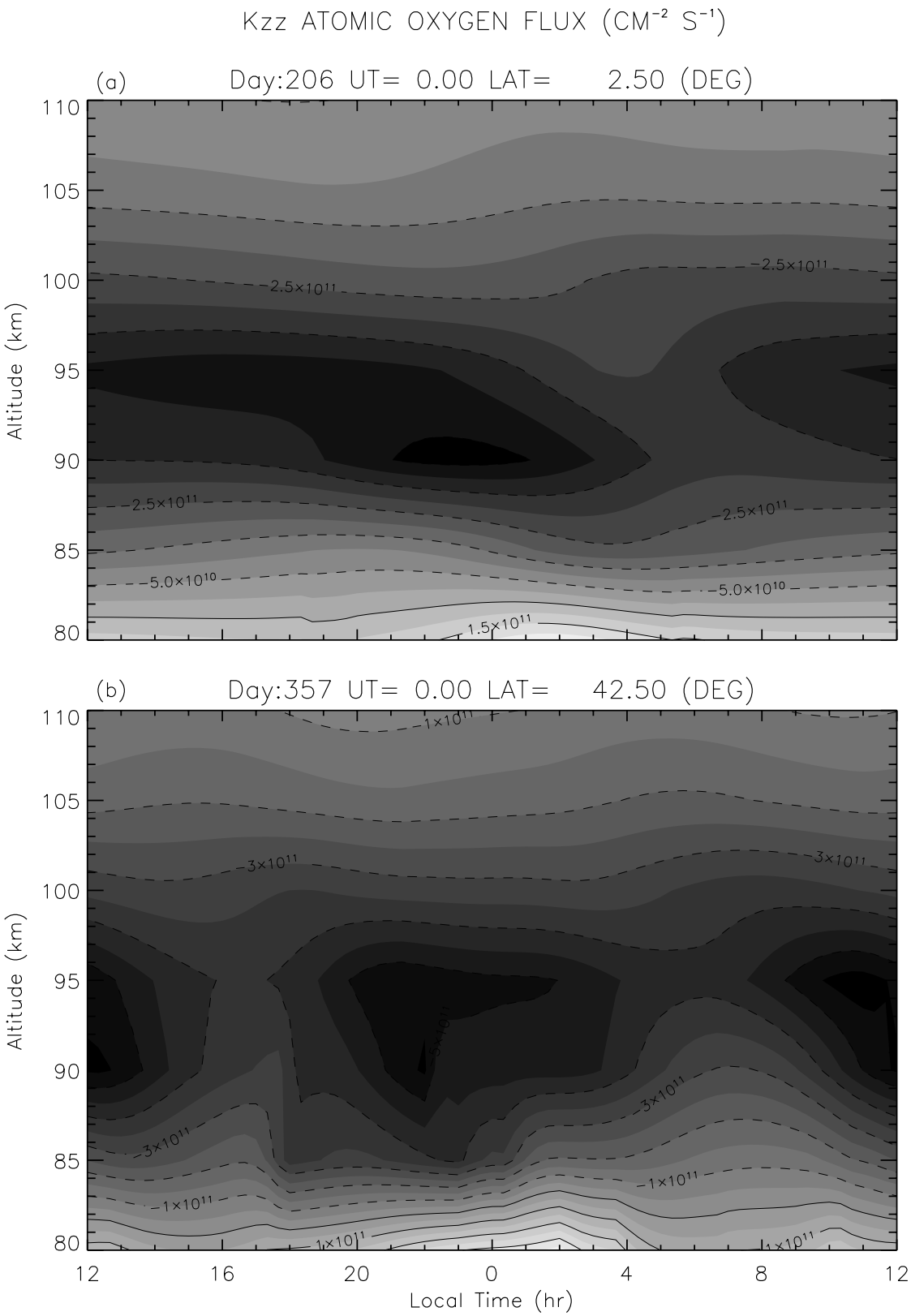

Figure 10: Atomic oxygen fluxes caused by eddy diffusion as from the TIME-GCM simulations for (a) 2.5º latitude on July 24, 1992, and for (b) 42.5º latitude on December 22, 1992.

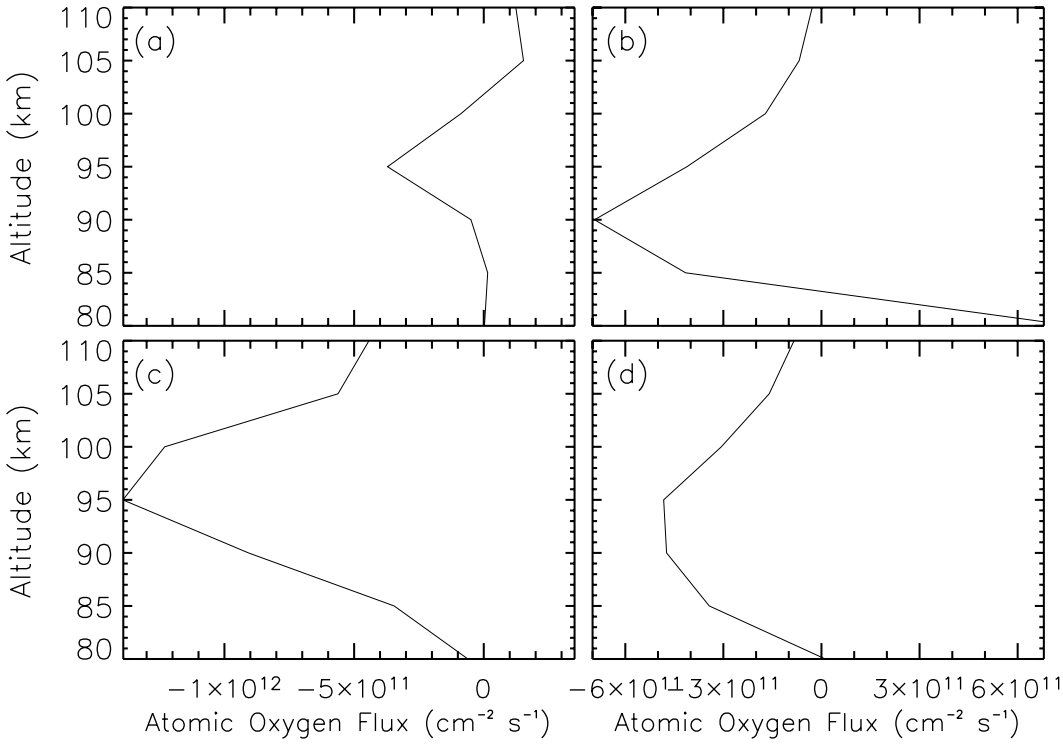

Figure 11: Daily averaged atomic oxygen flux at 62.5º latitude from the TIME-GCM simulations for (a) July 24, 1992 due to vertical advection, (b) July 24, 1992 due to eddy mixing, (c) December 22, 1992 due to vertical advection, and (d) December 22, 1992 due to eddy mixing. The top two panels are for the fluxes for the summer and the bottom two are for the winter; the left two panels are for the fluxes due to vertical advection and the right two are due to eddy diffusion.

	J	F	M	A	M	J	J	A	S	O	N	D
1991											4(13)	12(9)
1992	10(7)	10(9)	15(7)	16(8)	17(8)	1	7(1)	16(9)	15(8)	18(6)	19(9)	15(9)
1993	22(8)	10(5)	16(8)	14(7)	18(9)	16(8)	18(6)	14(8)	11(5)	2(1)	17(4)	15(6)
1994	21(8)	20(9)	24(15)	5(5)	1	7(8)	7	9	6(4)	10(10)	4(1)	6
1995	13(5)	20(8)	13(7)	4(3)		2(1)	8(6)	5	15	19	17	13
1996	29	14	13	5	2		2	8	10	6	14	8(1)
1997	5	7	14(14)	7(8)				4(2)				
Total	100 (28)	81 (31)	95 (51)	51 (31)	38 (17)	26 (17)	42 (13)	56 (19)	57 (17)	55 (17)	75 (27)	69 (25)

Table 1: Numbers of days of WINDII observations for the O(^{1}S) and OH (in parentheses) nighttime airglow emissions through 1991-1997.